JOURNAL OF COMPUTATIONAL PHYSICS 88, 409–432 (1990)

Fast Moving Sub-subsonic Shocks in Closed-End Tubes

M. VALORANI AND M. DI GIACINTO

Dipartimento di Meccanica e Aeronautica,
Università degli Studi di Roma "La Sapienza", Via Eudossiana 18, Rome 00184, Italy

Received November 11, 1987; revised June 30, 1989

The problem of the detection, formation, and propagation of a fast moving shock in a wholly subsonic environment inside a closed-end tube is solved by a finite-difference integration method belonging to the family of shock-fitting techniques. The shock is fitted by locally combining the method of characteristics with the Rankine–Hugoniot relations, while the regions of smooth flow are solved via a λ scheme. A special attention is devoted to the problems related to shock detection and formation and to the treatment of the reflection of the shock at the boundaries. The pressure oscillation data demonstrate that the shock transition remains sharp and oscillation-free even after many wave cycles. The spectral analysis performed on these data shows that the energy distribution among modes is in good agreement with the analytical solution. These results point out the characteristics of low dissipation and dispersion of the method. For these reasons, the proposed integration technique is particularly well suited for the study of nonlinear axial mode instabilities (usually referred to as "triggered instabilities") in combustion chambers.

1. INTRODUCTION

In a large number of classical problems, a steady or slow-moving shock separates a region of supersonic flow from a region of subsonic flow. Conversely, if an initial pressure perturbation is prescribed within a tube, closed at both ends, a shock wave may appear, which moves rapidly within a wholly subsonic environment. The numerical analysis of the formation of a shock and of its subsequent evolution and multiple reflections at the end-walls of the tube is a challenging task, from which a better understanding of basic relations between physics and numerics can be gained.

Baum and Levine [1] provided an excellent numerical description of the problem after conducting an exhaustive comparative study of several shock-capturing techniques. Their final goal was the definition of a technique suited for the analysis of nonlinear axial mode instabilities in combustion chambers [2, 3], for which the occurrence of numerically induced pre- and post-shock oscillations "does not just impair the accuracy of the solution, but it can lead to non-physical solutions by erroneously 'triggering' nonlinear combustion instabilities" [1]. Here, we

0021-9991/90 $3.00

intend to supplement their review by the application of a shock-fitting technique to this problem.

A suitable integration method to be coupled with shock-fitting is the λ scheme [4, 5]. Since all schemes analyzed in [1] discretize the equations of motion in divergence form, whereas the proposed technique is a finite-difference interpretation of the method of characteristics, we have to prove that results obtained by the present method are at least as good as the best results of [1].

For a wholly subsonic environment, indeed, the marriage of the λ scheme with shock-fitting is not as straightforward as it may appear in [5], where transonic or wholly supersonic environments are analyzed. The general description of the technique is given in Sections 4–8.

Special points of interest of the technique are (i) the numerical handling of the shock detection (Section 10), (ii) the updating of points neighboring the shock (Section 9), and (iii) the treatment of the reflection of the shock at the end-walls of the tube (Section 11).

In the discussion of the results (Section 12) particular attention has been given to the problems associated with shock detection (12.2), shock formation (12.3), and reflection (12.4). We conclude our study with a spectral analysis of the pressure oscillations at a fixed location (Section 12.5). Comparison of our power spectral densities with the results of [1] shows excellent agreement.

2. Generalities of the Method

Richtmyer and Morton [6] discussed a theoretical formulation for fitting an embedded shock, but they did not made any computation based on that theory. The first computations have been made by Moretti and Abbett [7] for blunt body flows. There, the shock was thought of as a boundary of the flowfield. From this first application to the latest ones dealing with two-dimensional unsteady flows with multiple embedded shock waves (Moretti [5]), a large amount of knowledge has been acquired in order to deal with both numerical and topological problems concerning shock wave propagation.

To solve this category of problems Salas [8] was the first to use a computational point free to float over a fixed grid ("floating shock point"). Later, Moretti and Di Piano [9] devised an unsteady one-dimensional computational technique to deal with many kinds of mutually interacting discontinuities.

Chern *et al.* [10], following a similar line of thought, tracked several kinds of singular surfaces (such as shock waves, contact discontinuities, slip lines, phase boundaries, chemical reaction fronts) by superposing on a fixed grid a lower dimensional adaptive grid associated with the evolving discontinuities.

The two approaches share the same basic philosophy, while they differ in the handling of the discontinuity evolution and in the range of applicability.

In our work, the "floating shock point" is a double-valued point representing the

states astride the shock discontinuity. This "shock point" can freely float on a fixed grid. The propagation of the "shock point" is described by coupling the method of characteristics with the Rankine–Hugoniot relations. The integration via characteristics is also applied for updating the "grid points" affected by the presence of the shock. The integration of the remaining "grid points" is performed by a finite difference scheme following the λ formulation.

The analogies between the present work and those mentioned above lie in the treatment of the smooth flow regions and in the updating of the position of the shock. This is carried out as in [9], while the computation across the discontinuity follows a procedure similar to that adopted by Chern *et al.* It must be noted that, unlike Moretti's or Chern's approaches, the value of the solution at "grid points" close to the shock is obtained by direct integration along characteristics as opposed, for example, to what is done in Chern's flux balances over the irregular cells close to the front.

Something which is apparently still missing in the "front tracking method" [10] is the ability to detect the onset of embedded discontinuities. Here, we propose a shock detection procedure that recalls, to some extent, the approach followed by Salas [8].

The search for a possible shock onset is confined at the grid cells where the characteristic slope decreases moving from one point to the next (compression regions). At the cell where the compression gradient is maximum, the presence of a shock is suspected, and the shock Mach number is approximated on the basis of the flow variable trends at the sides of this cell. Depending on the value of the Mach number obtained in this way, the actual presence of the shock in the cell is assumed or not. A low value of the minimum shock Mach number permits the shock detection at a very early stage of the shock development. This criterium is easy to implement, numerically inexpensive, and it allows the detection of any kind of unsteady shock (super–sub, super–super, and sub–sub).

Procedures similar to that exposed above have also been applied by the authors in quasi-one-dimensional problems with multiple discontinuity interactions [11] and in two-dimensional unsteady problems [12].

3. The Problem

A closed-end tube is filled with a gas at rest. The gas is assumed ideal, inviscid, and non-conducting. When an initial pressure perturbation is applied, the gas is set into motion. The propagation of pressure waves has a strong nonlinear character that leads to the steepening of pressure gradients. Eventually, the isotropic solution will develop a multi-valued region in the (x, t) plane. The flow at this point cannot remain isentropic anymore and a shock discontinuity develops. The problem of finite amplitude sound wave propagation in an unbounded medium is described in [13]. There, it is shown that the flow eventually reaches a stable sawtooth-like shape. Inside the tube the shock travels back and forth reflecting at the ends. There

is a conversion of energy into heat any time a fluid particle passes through a shock and at any reflection. This makes the amplitude of the pressure perturbations decay, following an exponential law.

In a real gas viscous and heat diffusion prevail over convection when the displacements of the fluid become smaller and smaller because of the loss of energy. When this occurs the shock wave decays into an ordinary wave.

4. Non-dimensionalization of Flow Variables

All quantities involved in the equations of motion are made dimensionless assuming the following values as reference,

$$p_r = 101325 \frac{N}{m^2}, \qquad x_r = 1\,m, \qquad \rho_r = 1.22 \frac{Kg}{m^3}, \qquad R_r = 287.05 \frac{J}{KgK},$$

where p is pressure, x is the spatial abscissa, ρ is density, R is the gas constant. The non-dimensional value of all remaining quantities can be obtained by dividing them by the values,

$$u_r = \left(\frac{p_r}{\rho_r}\right)^{1/2}, \qquad a_r = u_r, \qquad t_r = \frac{x_r}{u_r}, \qquad T_r = \frac{p_r}{\rho_r R_r},$$

where u is flow velocity in the x-direction, a is speed of sound, t is time, T is absolute temperature.

In order to simplify the form of the equations of motion, the non-dimensionalizing value of the entropy S is assumed equal to γR_r. The entropy is set equal to zero at (T_r, p_r). Note also that the non-dimensional time in our results differs from that in [1], since we used as reference velocity $u = (p_r/\rho_r)^{1/2}$, instead of $a = (\gamma p_r/\rho_r)^{1/2}$. Hence, the two non-dimensional time are related as follows:

$$t_{[1]} = t_{p.w.} \gamma^{1/2}.$$

5. One-Dimensional Equations of Motion and Boundary Conditions

The equations of a one-dimensional unsteady inviscid flow, for a perfect gas, can be written in quasi-linear form as

$$\mathbf{w}_t + J\mathbf{w}_x = 0 \tag{1}$$

with

$$\mathbf{w} = \begin{Bmatrix} a \\ u \\ s \end{Bmatrix}, \qquad J = \begin{bmatrix} u & \delta a & 0 \\ \dfrac{a}{\delta} & u & -a^2 \\ 0 & 0 & u \end{bmatrix}. \tag{2}$$

The matrix J can be diagonalized as $J = L^{-1}\Lambda L$, with

$$L = \begin{bmatrix} \frac{1}{\delta} & 1 & -a \\ \frac{1}{\delta} & -1 & -a \\ 0 & 0 & 1 \end{bmatrix}, \qquad \Lambda = \begin{bmatrix} u+a & 0 & 0 \\ 0 & u-a & 0 \\ 0 & 0 & u \end{bmatrix}. \tag{3}$$

Hence (1) become

$$L\mathbf{w}_t + \Lambda L\mathbf{w}_x = 0, \tag{4}$$

obtained by left-multiplying (1) by L. The diagonal terms of Λ are the eigenvalues of J, while L is the matrix of the left-eigenvectors of J.

Introducing the notations

$$R_1 = \frac{a}{\delta} + u, \qquad R_2 = \frac{a}{\delta} - u, \qquad \lambda_1 = u + a, \qquad \lambda_2 = u - a, \qquad \lambda_3 = u, \tag{5}$$

we can write (4) in the form used for the integration at the "grid points" via λ scheme,

$$\begin{aligned} S_t + \lambda_3 S_x &= 0 \\ R_{1t} + \lambda_1(R_{1x} - aS_x) - aS_t &= 0 \\ R_{2t} + \lambda_2(R_{2x} - aS_x) - aS_t &= 0, \end{aligned} \tag{6}$$

and, for the shock fitting device, these equations can be rewritten as

$$\begin{aligned} \frac{DS}{Dt} &= 0 \qquad \text{along } \lambda_3 \\ \frac{DR_1}{Dt} - a\frac{DS}{Dt} &= 0 \qquad \text{along } \lambda_1 \\ \frac{DR_2}{Dt} - a\frac{DS}{Dt} &= 0 \qquad \text{along } \lambda_2. \end{aligned} \tag{7}$$

The tube has closed ends. The fluid velocity at the boundaries is zero. Therefore the entropy, which is convected along pathlines, can be varied at the boundaries only by the reflection of the shock. Signals travelling along the characteristics λ_1 or λ_2 are simply reflected at the boundaries.

6. Integration of Equations of Motions at Grid Points

"Grid points" are updated in time by applying the version of the λ scheme presented in [9]. The scheme follows a predictor–corrector procedure. It is second-

order accurate in space and in time even for non-linear problems [14]. When the Courant number is set equal to 1 or 2, the scheme is essentially non-dissipative and non-dispersive. The CFL condition is applied by taking into account not only the wave propagation speeds at "grid points", but also those at the "shock points".

The one-dimensional, two-level scheme can be written as follows:

Predictor step. Let $x = n\,\Delta x$, $t = k\,\Delta t$, and

$$\begin{aligned} f^k_{1,n} &= -\frac{1}{4\,\Delta x}(\lambda^k_{1,j} + \lambda^k_{1,j'})(R^k_{1,j'} - R^k_{1,j}) \\ &\quad - [(a\lambda_1)^k_j + (a\lambda_1)^k_{j'}](S^k_{j'} - S^k_j) \\ f^k_{2,n} &= -\frac{1}{4\,\Delta x}(\lambda^k_{2,j} + \lambda^k_{2,j'})(R^k_{2,j'} - R^k_{2,j}) \\ &\quad - [(a\lambda_2)^k_j + (a\lambda_2)^k_{j'}](S^k_{j'} - S^k_j) \\ f^k_{3,n} &= -\frac{1}{4\,\Delta x}(u^k_j + u^k_{j'})(S^k_{j'} - S^k_j). \end{aligned} \tag{8}$$

The index j in the i-th equation of the set (8) equals $n-1$ when the corresponding $\lambda_{i,n}$ is positive, otherwise j is set equal to n. The index j' is always defined as $j' = j+1$.

Corrector step. Let also

$$\begin{aligned} F^{k+1/2}_{1,n} &= 2f^{k+1/2}_{1,n} - f^k_{1,j} \\ F^{k+1/2}_{2,n} &= 2f^{k+1/2}_{2,n} - f^k_{2,j} \\ F^{k+1/2}_{3,n} &= 2f^{k+1/2}_{3,n} - f^k_{3,j}, \end{aligned} \tag{9}$$

where j equals $n-1$ when the corresponding $\lambda_{i,n}$ is positive, otherwise j is set equal to $n+1$.

Knowing all the values at level k, the values at level $(k+\frac{1}{2})$ are obtained as follows:

$$\begin{aligned} S_t &= f^k_{3,n}, \qquad S^{k+1/2}_n = S^k_n + S_t\,\Delta t \\ a^{k+1/2}_n &= a^k_n + \left[\delta a S_t + \frac{\delta}{2}(f^k_{1,n} + f^k_{2,n})\right]\Delta t \\ u^{k+1/2}_n &= u^k_n + \tfrac{1}{2}(f^k_{1,n} - f^k_{2,n})\,\Delta t. \end{aligned} \tag{10}$$

At the second level similar equation are used, with F instead of f and $(k+\frac{1}{2})$ instead of k.

Since the scheme discretizes equations written in quasi-linear form, it is not able to provide a built-in mechanism for the evaluation of shocks. Any "physical" shock

is turned by the scheme into an isentropic jump, moving at an incorrect speed, across which the Rankine–Hugoniot relations are not satisfied. This scheme does not preserve the monotonicity of the solution; therefore, oscillations may appear in regions of strong gradients.

7. Integration of Compatibility Equations along Characteristics

The shock-fitting device consists of solving the double-valued "shock point" and the "grid points" affected by the closeness of the shock, by applying a numerical scheme of integration based on (7).

The compatibility equations (7) are discretized as follows. Let x_P be the abscissa of a point at the time level t^{k+1}, to be updated by applying (7). Let C_1, C_2, C_3 be the points of intersection of the characteristics passing through P with any time-like arc QR in the (x, t) plane (Fig. 1).

We will assume the characteristics to be straight lines within a time interval. A first-order discretization of (7) can be written as

$$S_{X_p}^{k+1} - S_{C_3} = 0 \tag{11a}$$

$$R_{1, X_p}^{k+1} - R_{1, C_1} = a_{C_1}(S_{X_p}^{k+1} - S_{C_1}) \tag{11b}$$

$$R_{2, X_p}^{k+1} - R_{2, C_2} = a_{C_2}(S_{X_p}^{k+1} - S_{C_2}). \tag{11c}$$

The new values of a and u at P are algebraically related to R_1 and R_2 through the relations (5).

Any point of intersection C_j of the arc QR with the characteristics λ_j passing through P can be determined by solving the system

$$\begin{aligned} &\lambda_j(x, t) = (x_P - x)/(t^{k+1} - t) \\ &F(x, t) = 0, \end{aligned} \tag{12}$$

where F defines the arc QR. The evaluation of any other function Φ along the arc

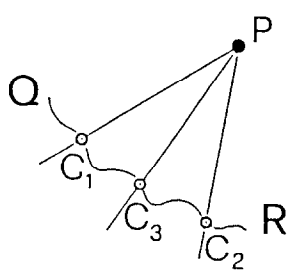

FIG. 1. Integration along characteristics.

QR is performed by assuming for Φ the same law of variation which have been used for $\lambda_j(x, t)$. The interpolating functions for λ_j will be defined in Sections 8 and 9.

The integration time step along characteristics at the "shock points" is defined as half the time step used for the integration at the "grid points".

8. Treatment of Shocks

The path of a discontinuity describes a straight line OP in the (x, t) plane (Fig. 2). The portions of the x-axis at the time level t^k, QO and OR, constitute two intersecting time-like arcs along which all variables are known. Equations (7) are integrated along characteristics coming from suitable points on QO and OR to update the states at points A and B.

Along arcs QO and OR a linear variation for $\lambda_j(x, t^k)$ is obtained by a least square fitting of the values of λ_j at three consecutive computational points (either "grid" or "shock points") belonging to QO (OR).

Let the low pressure side of the double-valued "shock point" be designated with A and the high pressure side with B. With respect to a frame of reference moving with the shock, the relative flow at A is always supersonic and at B is always subsonic. Hence three pieces of information are convected to A along characteristics coming from OR and only one arrives in B starting from QO. The Rankine–Hugoniot relations applied between A and B, provide the three extra relations necessary for calculating the states astride the shock and its velocity.

The updating of the shock Mach number $M_s = (u_A - w)/a_A$, where w is the shock speed, is performed by using a linearized procedure.

Let Σ be defined as a function of the shock Mach number [5, 15],

$$\Sigma = \frac{(R_{jB} - R_{jA})}{a_A} = \frac{\Sigma^* - 1}{\delta}, \tag{13}$$

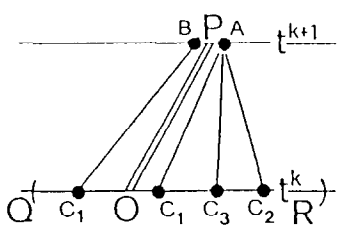

FIG. 2. Treatment of shock.

where j is set to 1 or 2 accordingly with the family of the shock and with

$$\Sigma^* = \frac{(a_B \pm \delta(u_B - u_A))}{a_A}$$

$$= \frac{[(\gamma M_s^2 - \delta)(1 + \delta M_s^2)]^{1/2}}{(1+\delta)\,|M_s|} \pm \frac{\delta(1 - M_s^2)}{(1+\delta)M_s},$$

where the plus sign has to be taken for $j=1$ and the minus sign for $j=2$.

The time derivative of Σ^*, is obtained using the chain rule,

$$\Sigma_t^* = \Sigma_{M_s}^* M_{s,t}.$$

Hence,

$$M_{s,t} = \frac{\Sigma_t^*}{\Sigma_{M_s}^*} = \frac{\delta \Sigma_t}{\Sigma_{M_s}^*}$$

with

$$\Sigma_t = \frac{(R_{jB,t} - R_{jA,t} - \Sigma a_{A,t})}{a_A}$$

and

$$\Sigma_{M_s}^* = \frac{\delta}{(1+\delta)M_s^2}\left\{\frac{M}{|M_s|}\,\frac{M_s^4 + 1}{[(M_s^2 - \delta)(1 + \delta M_s^2)]^{1/2}} \mp (1 + M_s^2)\right\}$$

with the minus sign for $j=1$ and the plus sign for $j=2$.

Finally,

$$M_s^{k+1} = M_s^k + M_{s,t}^k\,\Delta t. \tag{14}$$

The values $R_{jA,t}$, $a_{A,t}$ can be accurately computed from the integration of (11) at the low pressure side. A small error is introduced in $R_{jB,t}$, where the entropy is assumed constant along λ_{jB}. A more accurate iterative procedure, taking into account even the small contribution of the entropy, is presented in [11].

The propagation speed of the shock needed to update the shock location is computed as

$$w^{k+1} = u^{k+1} - a^{k+1} M_s^{k+1}. \tag{15}$$

9. Updating of Grid Points around the Shocks

A further remark concerns the integration of the "grid points" neighbouring a discontinuity. The integration via λ scheme may be erroneously carried out when

the domain of dependence forces some x-derivatives to be computed across the discontinuity. This situation may occur for those "grid points" just swept by the moving shock. When this happens, the integration at those single points is performed by using the compatibility equations (7).

Because of the proximity of the shock, it is very likely that some backward characteristics stemming from X intersect the shock at time levels successive to t^k (Fig. 3).

When this happens, a linear variation of λ_j (and of all other functions) along the time-like arc PO is assumed. The flow variables in P are known since the shock is solved as a first step of the integration procedure.

It should be pointed out that the integration of X-type points performed accordingly to the procedure described above greatly enhances the precision and the robustness of the calculation, becoming in this way one of the most significant features of the method. Any kind of interpolation or, even worse, extrapolation used for the computation of points such as X makes the code less accurate and more dissipative; sometimes it may lead to catastrophic instabilities.

10. Shock Detection

Any shock-fitting device needs some criteria for determining when and where it is no longer possible to treat a compression wave as an isentropic process. Analytically, a shock wave appears when characteristics of the same family overlap. This occurrence is interpreted in the discretized model by pinpointing a cell in the (x, t) plane where a shock is likely to form. We use a cascade of tests for this purpose:

(a) A shock can occur only in compression waves, i.e. regions where characteristics of the same family converge. This happens to be the case when

$$\frac{d\lambda_1}{dx} < 0 \quad \text{if} \quad \frac{dp}{dx} < 0$$

or when

$$\frac{d\lambda_2}{dx} < 0 \quad \text{if} \quad \frac{dp}{dx} > 0.$$

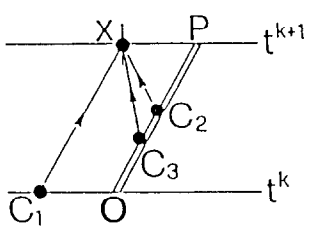

FIG. 3. Updating of X-type points next to the shock.

(b) Inside the compression region, we locate the possible shock where the compression gradient is the steepest, i.e., where

$$\frac{d^2\lambda_1}{dx^2}=0 \qquad \text{if} \quad \frac{dp}{dx}<0$$

or, where

$$\frac{d^2\lambda_2}{dx^2}=0 \qquad \text{if} \quad \frac{dp}{dx}>0.$$

(c) An estimate of the strength of the candidate shock is needed. A measure of strength is the shock Mach number $M_s=(u_A-w)/a_A$, where the shock speed w is estimated as the mean value of the characteristics at the two nodes bracketing those cells that have been passed tests (a) and (b),

$$w=(\lambda_{j,n}+\lambda_{j,n+1})/2, \tag{16}$$

where j is chosen accordingly with the family of the onsetting shock. The values of u_A and a_A are evaluated as follows: when a "shock point" is created, a small jump, of rather arbitrary size, is superposed on the solution, consistent with a new discretized description of the solution. In order to reduce as much as possible the arbitrariness of the jump estimate, the initial values in front of the shock are defined as a fraction of the whole jump between the two nodes of the cell:

$$\begin{aligned} a_A &= a_n+\alpha(a_{n+1}-a_n) \\ u_A &= u_n+\alpha(u_{n+1}-u_n), \end{aligned} \tag{17}$$

where α is less than $\frac{1}{2}$ (typically $\alpha=0.45$). At this point an approximate value of M_s can be computed and when this value exceeds a given threshold, say $M_{\min}$, we decide that a shock is born at the middle of that cell.

The crucial steps for a correct shock formation are an early detection and a proper placement of the shock. The failure of the first requirement is responsible for the development of strong wiggles, whose effects cannot be eliminated anymore. An incorrect placement leads to the tracking of a simple compression wave instead of a true shock.

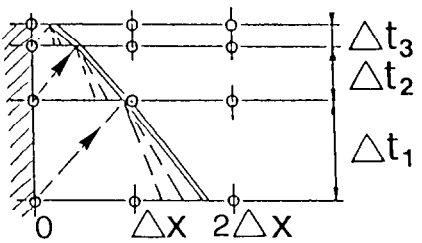

FIG. 4. Reduction of time step when shock approaches the boundary.

11. Shock Reflection

So far, we have described the treatment of a shock when it has no interaction with the boundaries. We have seen that the solution of (7) requires the existence of time-like arcs along which an initial solution of (7) is known. Hence, the updating of a "shock point" P, from the time level t^k to t^{k+1}, is possible only when no point of intersection C_j falls outside the boundaries. In Fig. 4, a left-running shock is approaching the left end of the tube.

The maximum allowable time step can then be defined by the intersection, in the (x, t) plane, of the least steep characteristics coming from the boundary with the shock path. When the shock approaches the boundary, the time step progressively decreases and when the distance from the boundary drops below a certain "small" value, say ε, we will proceed to compute the reflection of the shock analytically (many classic text books [16, 17], report all pertinent details).

12. Discussion of Results

The evolution of a pressure perturbation in a closed-end tube provides an excellent test case for analyzing the efficiency of the proposed numerical methods in the description of shocks moving in wholly subsonic flowfields. In the following sections the initial conditions for the test case will be specified and then the behaviour of the numerical simulation with respect to the shock detection, formation, and reflection will be discussed in depth. Finally, the evolution of the pressure oscillation will be analyzed both in the time and frequency domain.

12.1 *Initial Conditions*

The pressure of the gas in the tube is initially set equal to $p_0 = 1$. The entropy is zero throughout the whole flow field. Then, a pressure perturbation $\tilde{p}(x) = \Delta p \cos(\pi x)$, is applied to the gas at rest. Tests are presented for values of $\Delta p = 0.2$ and 0.6. The ratio of specific heats is set equal to 1.22 in order to agree with the value used by Baum and Levine [1]. The Courant number is always set equal to 0.9. Results are presented for meshes having 64 and 128 intervals, respectively.

12.2. *Shock Detection*

The effects of a delayed shock detection are evidenced in Fig. 5e, where $M_{\min} = 1.044$ and $\Delta p = 0.6$. The λ scheme treats the strong gradients, associated with the development of a discontinuity in the solution, as an "isentropic shock".

FIG. 5. (a)–(d) Isomach lines in the (x, t) plane; squares trace the shock path. (e)–(h) Velocity profile time evolution; solid lines bracket the velocity jump across the moving shock, arrows show the versus of increasing time. (a), (e) No tracking: development of an "isentropic jump," (b), (f) Early shock detection, $M_{\min} = 1.0015$. (c), (g) Delayed shock detection, $M_{\min} = 1.008$, (d), (h) Mesh dependence of the pre-shock wiggle.

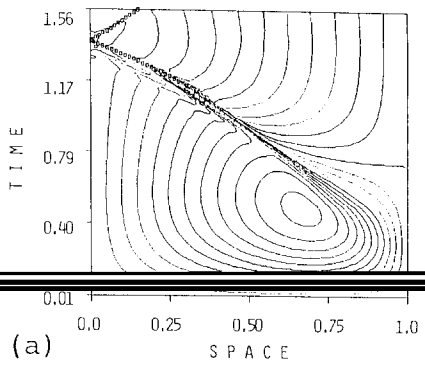
1.56
1.17
0.79
0.40
0.01
TIME
0.0
0.25
0.50
0.75
1.0
SPACE

(a)

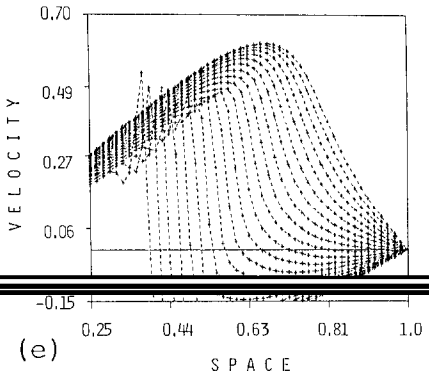
0.70
0.49
0.27
0.06
-0.15
VELOCITY
0.25
0.44
0.63
0.81
1.0
SPACE

(e)

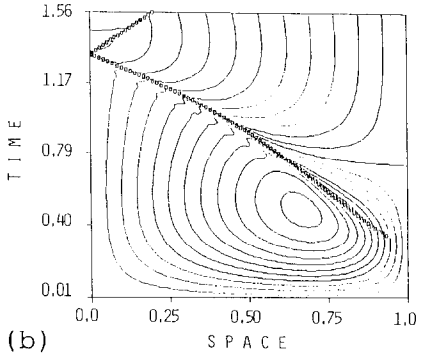
1.56
1.17
0.79
0.40
0.01
TIME
0.0
0.25
0.50
0.75
1.0
SPACE

(b)

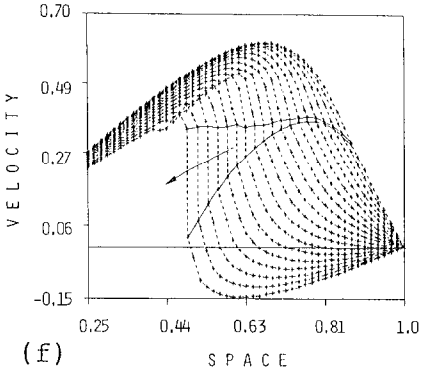
0.70
0.49
0.27
0.06
-0.15
VELOCITY
0.25
0.44
0.63
0.81
1.0
SPACE

(f)

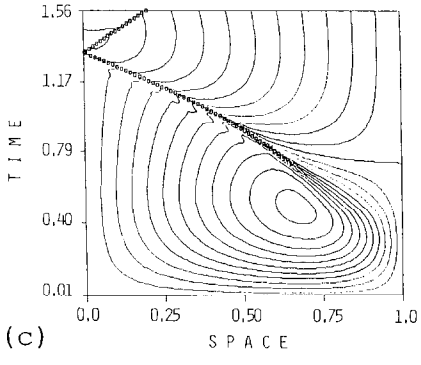
1.56
1.17
0.79
0.40
0.01
TIME
0.0
0.25
0.50
0.75
1.0
SPACE

(c)

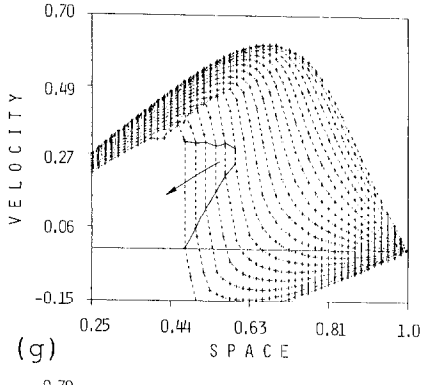
0.70
0.49
0.27
0.06
-0.15
VELOCITY
0.25
0.44
0.63
0.81
1.0
SPACE

(g)

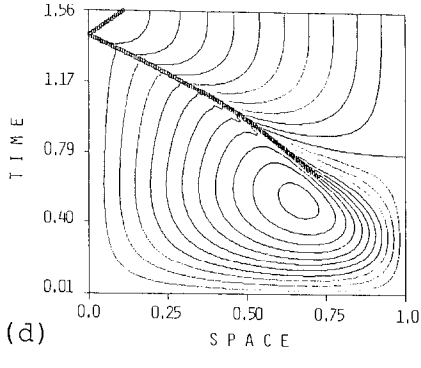
1.56
1.17
0.79
0.40
0.01
TIME
0.0
0.25
0.50
0.75
1.0
SPACE

(d)

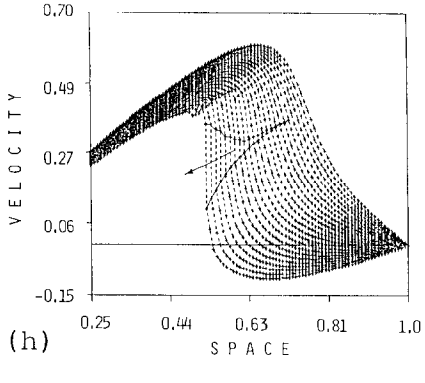
0.70
0.49
0.27
0.06
-0.15
VELOCITY
0.25
0.44
0.63
0.81
1.0
SPACE

(h)

It is clear from Fig. 5e, that the scheme does not preserve the monotonicity at the jump and that the "isentropic shock" moves with an incorrect speed (Fig. 5a).

Two solutions are presented where smaller $M_{\min}$ are adopted (Figs. 5b, f, and 5c, g). The trace of the shock is marked with squares in the (x, t) plots of Figs. 5a–d. Solid lines in plots of u vs x at successive instants (Figs. 5f–h) bracket the shock growth.

It is evident that a smaller $M_{\min}$ allows an earlier detection of the shock (compare Figs. 5b and c). The figures show that solutions obtained with different $M_{\min}$, providing that $M_{\min}$ is small enough, do not substantially differ.

It can also be observed that the shock evolution immediately after detection behaves rather smoothly no matter the $M_{\min}$ chosen.

12.3. *Shock Formation*

Problems, under the form of a pre-shock oscillation, arise prior to shock appearance and formation. By a comparison of Figs 5b, f (obtained with 64 intervals) with Figs. 5d, h (obtained with 128 intervals) it seems that the magnitude of this wiggle decreases with finer meshes; it seems also independent from the value chosen for $M_{\min}$ (see Figs. 5b, c).

The development of this oscillation is the result of a loss in accuracy that the onsetting shock induces in the solution. The accuracy of a discretized scheme is strictly related to the existence of a uniformly convergent Taylor expansion of the solution and, consequently, to the location of singularities of such solution, considered as a function of a complex variable.

If a singular point of the solution moves towards the real axis, a local lack of convergence may occur. Near the edge of the domain of convergence the leading terms of the Taylor series appear to form a divergent sequence, The discretized scheme, built by neglecting the higher order terms of the Taylor series, introduces a local error that grows as the singular point gets closer to the real axis (i.e., when a shock jump is about to appear in the solution). The discretized solution can converge only in the mean, not uniformly (see other details in [19]).

Once a shock is fitted, the computational domain is actually split in two parts. The shock becomes merely the boundary across two regions, whose correspondent singular point tend to move away from the real axis as the shock, by increasing its strength, absorbes the region of steep gradients characterizing the compression wave around the shock.

A Fourier expansion of the solution when the shock is about to form, or just fitted, displays a progressively increasing energy content at the higher modes. Now, a second-order upwind scheme introduces a phase shift error that is a function of the wave number. This fact can also be observed by analyzing the propagation of a truncated sine wave. In this case the presence of many harmonics in the solution is introduced by replacing the original wave with the sum of a finite number of harmonic components (and this is always the case when a discretized representation of the function is adopted). A second-order upwind scheme under these conditions

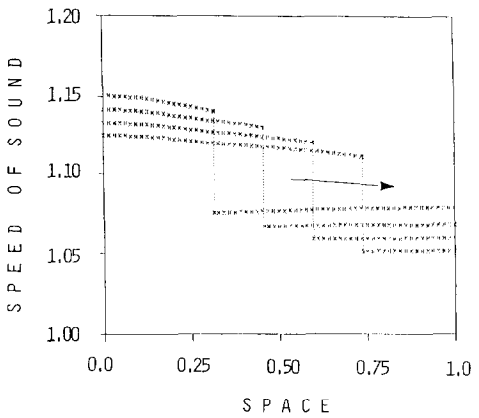

FIG. 6. Fully-developed rightward moving shock.

develops a precursor that looks quite similar to that exhibited by our present results [20].

In fact, perhaps the most appealing feature of a shock fitting approach lies specifically here: after the fitting, the flowfield at both side of the shock can become smooth again, recovering uniform convergence with a low energy content at the higher harmonic components. At this point the discretized scheme does not pose problems any longer in properly describing the evolution of the solution.

In any case, it must be noted that the pre-shock wiggle disappears when the shock becomes fully developed, having affected the calculation only momentarily, as it is demonstrated by Fig. 6 where the shock propagates with little dissipation and dispersion (in Fig. 6 the jump on the speed of sound moves rightward).

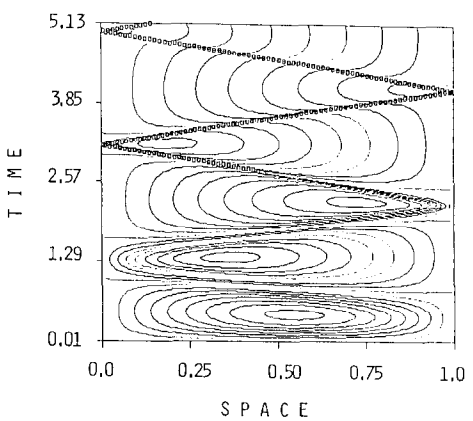

FIG. 7. Reflections of a partially shocked compression wave.

12.4. *Shock Reflection*

When the amplitude of the initial pressure perturbation drops below 0.2, the shock needs a longer time to reach its fully-developed state shown in Fig. 6. The compression wave reflects two times (Fig. 7) and only the third time it is partially shocked (Figs. 8a, b). Solid lines bracket the velocity jump approaching (Fig. 8a) and leaving (Fig. 8b) the left end of the tube. In Fig. 8c, d, lines of constant Mach number are plotted on an enlarged (x, t) scale in the vicinity of the shock reflection. The flowfield in front of the shock, zone (2), is far from being uniform. Therefore, an error is introduced if the shock is still far from the boundary (Fig. 8c), since the shock reflection is computed on the basis of the values at the low pressure side (Section 8). This error can be gauged by the relative increase of the shock Mach number from A to B, which is 1.52 % in Fig. 8c and 0.19 % in Fig. 8d. The long term effect of such inaccuracies are illustrated in Figs. 8e, f, where the overall mass loss of the system due to numerical errors is shown. The two results refer respectively to a limiting value of $\Delta x/\varepsilon = 4$ (Fig. 8e) and $\Delta x/\varepsilon = 256$ (Fig. 8f). During the initial stage of the transient (AB, Fig. 8e) it is the basic λ scheme that dissipates. The losses increase slightly right after the reflection of the compression wave (A_1, A_2). The fitting of the shock occurs around point B. The shock formation phase falls between B and C and in C the first shock reflection occurs. An inaccurate shock reflection is not conservative, as measured by the sharp jump CD in Fig. 8e. In Fig. 8f the size of the jump CD has almost vanished. Comparing the two results shows how much the accuracy of the computation is affected by the shock reflection. The results also demonstrate that the gain in accuracy obtained by an accurate shock reflection always overcome the extra losses due to the temporary reduction of the time step needed to perform such accurate reflection (see Section 11). The result in Fig. 8f also shows that the overall mass loss after 3691 iterations is of about 0.7 %.

12.5. *Overall Solution*

Different features are associated with the 20 % and the 60 % initial pressure perturbation cases. In the following, shock formation, damping, and long term behavior in the two cases will be compared.

Shock formation. The rate of growth of the 20 % case (Fig. 8a) is obviously lower than that of the 60 % case (Fig. 5f). It has already been observed that the compression wave in the 20 % case needs three reflections before it reaches a partially shocked state (point S in Fig. 9b), while in the 60 % case the shock is almost fully developed already at the first reflection (point S in Fig. 9e). The method encounters different difficulties in the two cases. In the 20 % case, the method should be able to follow regions with strong compression gradients for a longer period, while in the 60 % case it should be able to handle the fast growth rate of the shock.

The presence of the pre-shock wiggle during the shock formation can be noted at point W in Fig. 9b. The disturbance is very small.

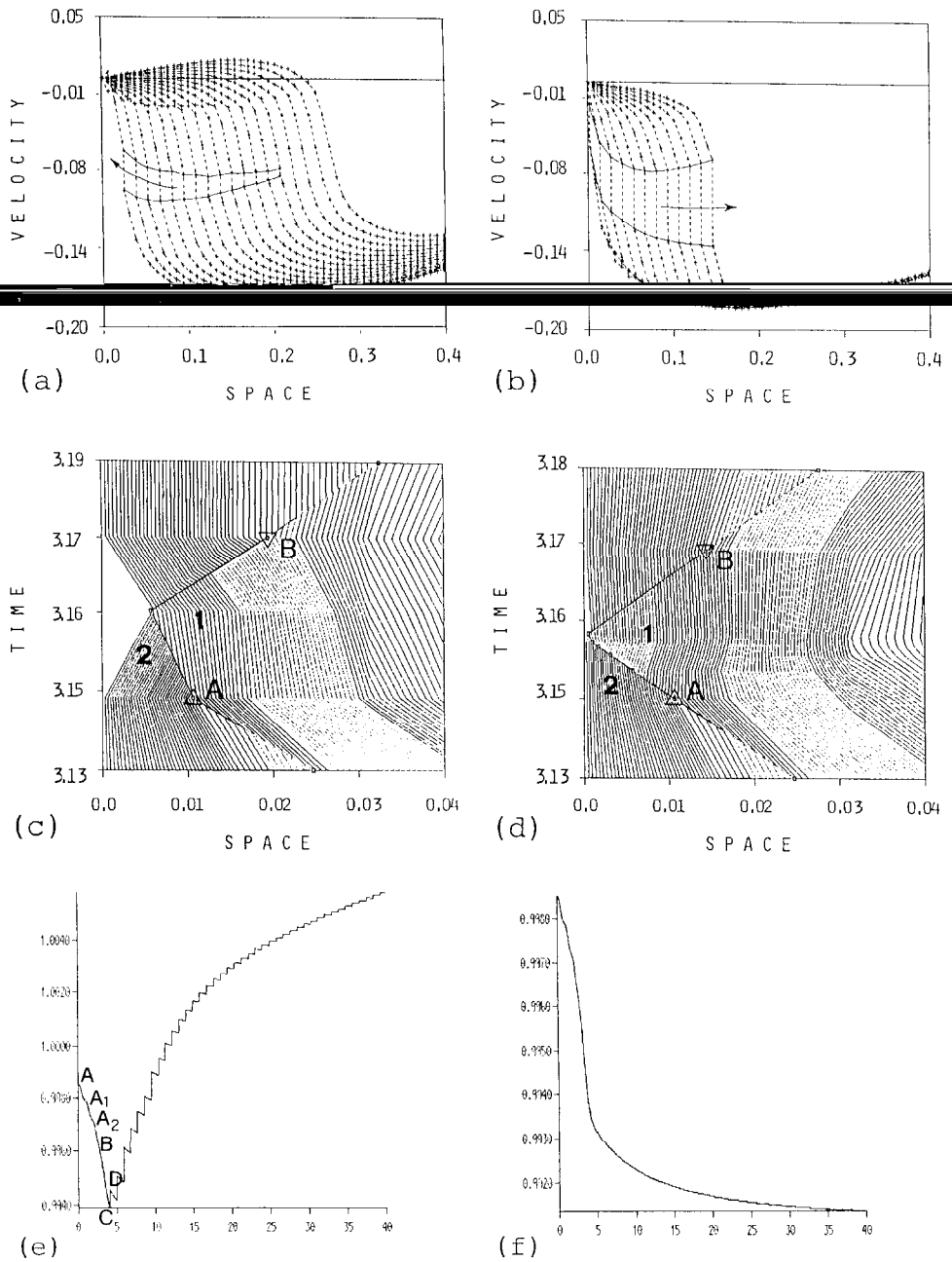

FIG. 8. Velocity profile time evolution before (a) and after (b) shock reflection. (c), (d) Enlarged plots of isomach lines in the vicinity of shock reflection: "far" reflection (c) and "close" reflection (d). (e), (f) Mass loss vs time obtained by computing the shock reflection accordingly with criteria shown in (c) and (d), respectively.

Note that the rarefaction wave in this initial phase is a curved line, for both the 20 % and the 60 % cases (Figs. 9b, e).

Damping. In Section 2, it has been mentioned that the shock looses strength by converting energy into heat. The damping coefficient ξ computed between the 6th and 30th oscillation in Fig. 9a and d, is about -0.0312 for the 20 % case and -0.0334 for the 60 % case. The value obtained for the 20 % case can be compared with the corresponding value in [1] ($LW+H+ACM$). The model of [1] seems to yield a slightly higher damping ($\xi = -0.0343$). For both numerical models (i.e., ours and $LW+H+ACM$), it is difficult to tell how much of the damping is due to physics and how much to numerics. This estimate becomes even more difficult for the model of [1], since use has been made of an artificial compression technique.

Long term results. The comparison of Fig. 9a with Fig. 10 of [1] shows that the 30th oscillation occurs almost at the same time ($t_{p.w.} = 53.85 \equiv (59.48)_{[1]}$). This indicates that wave propagation speeds in the two models are roughly the same. The numerical results of Fig. 9c, f can be qualitatively compared with the plot of the analytic sawtooth-like function exponentially damped, shown in Fig. 9g. The damping of this function is set equal to -0.033, the initial amplitude is 0.2, the period 1.8. These parameters have been chosen in order to give a good fitting of the computed and analytical results between time 50 and 60. The comparison indicates that (i) the computed solution after about 5000 steps preserves a perfectly sharp and oscillation-free shock and (ii) the expansions between shocks are represented by straight lines as in the analytical solution of Fig. 9g.

Spectral analysis. The time evolution of the pressure oscillation is analyzed by an FFT routine. The results are presented, following [18], as plots of W/σ^2 vs frequency, where

$$W(f) = 4\pi S(\omega), \tag{18}$$

$$0 < f < +\infty, \qquad \text{and} \qquad -\infty < \omega < +\infty.$$

Here, $S(\omega)$ is the power spectral density (PSD), σ^2 the variance of the sampled data.

Accumulated PSD data vs frequency, are also presented. They give the energy content up to the frequency f:

$$\int_0^{\bar{f}} \frac{W(f)}{\sigma^2}\, df = 4\pi \int_{-\bar{\omega}}^{\bar{\omega}} \frac{S(\omega)}{\sigma^2}\, d\omega.$$

FIG. 9. All figures show time evolution of pressure oscillations at an end of the tube. (a)–(c) Results for an initial amplitude of 20 % of mean pressure, and (d)–(f) for an amplitude of 60 %. (g) Results for a sawtooth-like damped function.

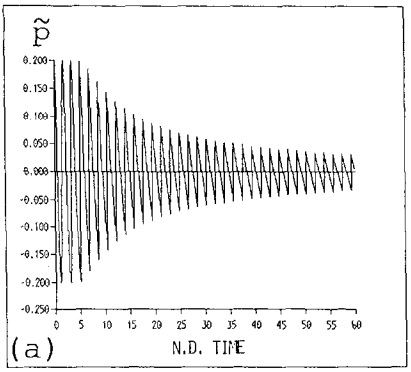
p̃
N.D. TIME
(a)

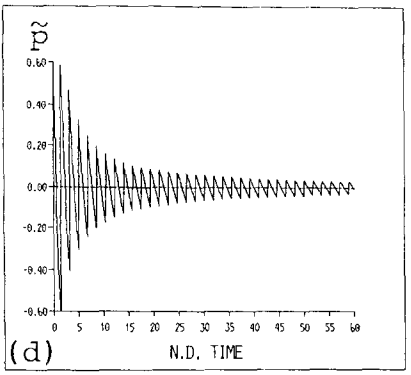
p̃
N.D. TIME
(d)

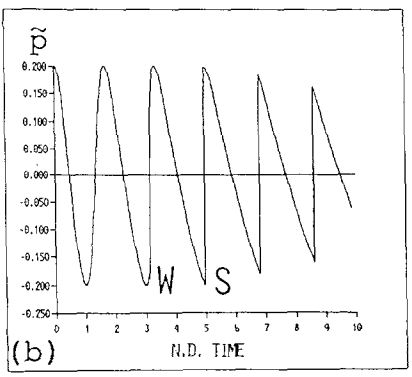
p̃
W
S
N.D. TIME
(b)

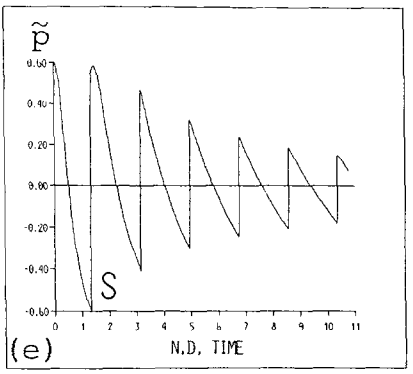
p̃
S
N.D. TIME
(e)

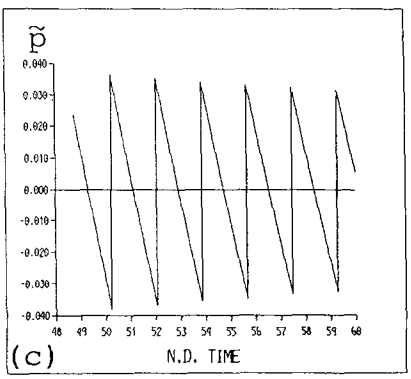
p̃
N.D. TIME
(c)

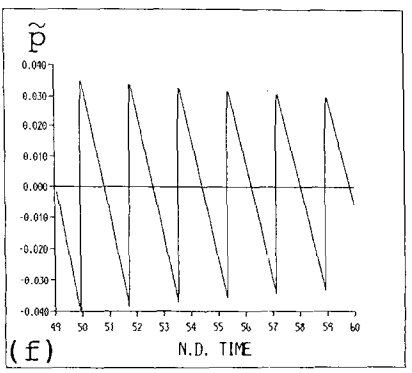
p̃
N.D. TIME
(f)

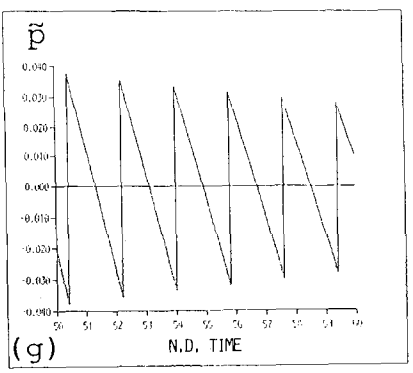
p̃
N.D. TIME
(g)

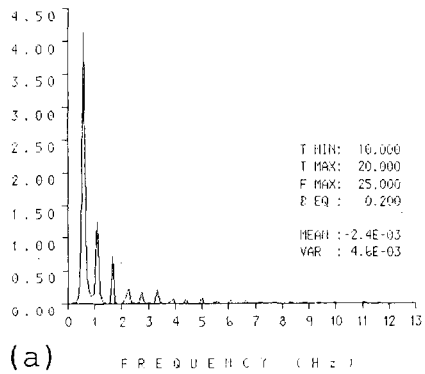

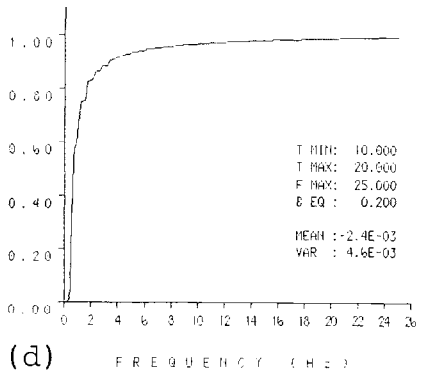

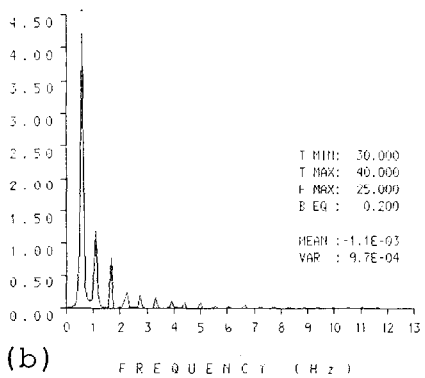

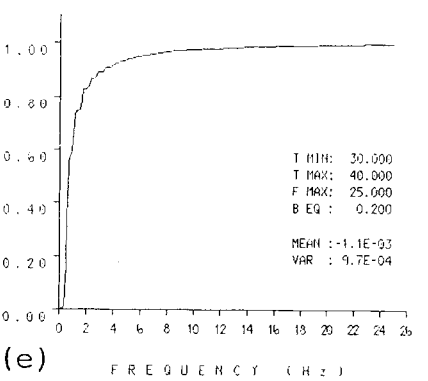

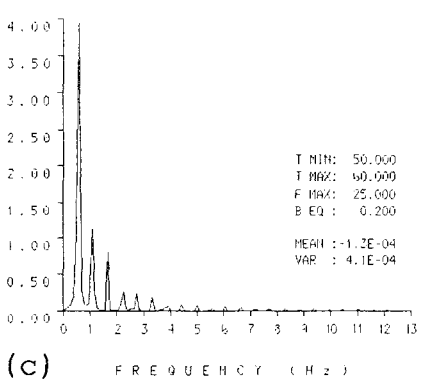

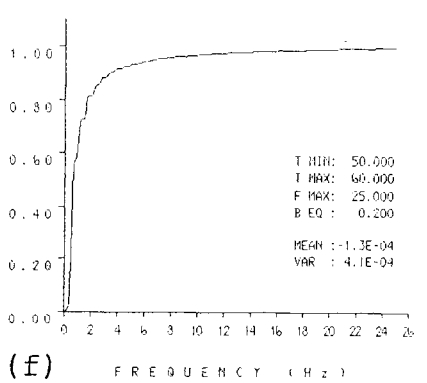

FIG. 10. Power spectral density for an initial amplitude of 20 % of mean pressure, obtained during time intervals 10–20 (a), 30–40 (b), 50–60 (c). (d)–(f) Accumulated PSD obtained from PSD data.

TABLE I

Energy Content among Harmonics

Analytic		Computed for t intervals		
Mode	$1/n^2$	10–20	30–40	50–60
1	1.0000	1.000	1.000	1.000
2	0.2500	0.223	0.224	0.239
3	0.1111	0.139	0.140	0.143
4	0.0625	0.059	0.062	0.059
5	0.0400	0.040	0.039	0.042
6	0.0277	0.035	0.035	0.036
7	0.0204	0.018	0.019	0.018
8	0.0156	0.017	0.016	0.017

Both the PSD and the accumulated PSD data, obtained on the 20 % case, demonstrate that up to 22 harmonics are already excited at the time interval from 10 to 20 (Fig. 10a, d). The PSD obtained at three successive time intervals, (Figs. 10a–c), show that the energy contained in the nth mode closely falls as $1/n^2$ with respect to the energy contained in the fundamental mode, as predicted analytically (Table I).

13. Conclusions

The possibility of adopting a shock-fitting approach to describe propagation of finite amplitude waves, wave steepening, and shock propagation in a closed end tube has been positively verified. The accurate treatment of the shock, represented by a floating double-valued point, and of the points affected by the presence of the shock, constitute the key features of this method. The non-dissipative and non-dispersive characteristics of the method are obtained without the need for "external" restoring of the high frequency content.

Results obtained for all initial amplitudes indicate that (i) shock transition remains oscillation-free even after many wave cycles, (ii) energy distribution among modes is in good agreement with the analytical solution, and (iii) it does not exhibit significant shifts among modes as time progresses.

The importance of an early shock detection and of the accurate computation of shock reflections have been demonstrated.

The characteristics summarized here above suggest that the proposed method is well tailored for the modelling of both combustion instabilities [1–3], and chemically reacting flows.

The extension to quasi-one-dimensional flows with multiple interactions among several kinds of discontinuities is feasible and it is presented elsewhere [11].

APPENDIX: List of Symbols

a, speed of sound (m/s)
CFL, Courant number
f, frequency (cycles/s)
J, Jacobian flux matrix
L, left-eigenvector matrix of J
M, Mach number
M_s, shock Mach number
$M_{\min}$, threshold value of M_s for shock detection
n, mode of oscillation
p, pressure (N/m^2)
$\tilde{p}$, pressure perturbation
R, ideal gas constant ($J/(KgK)$)
R_j, Riemann variables along characteristics
S, entropy (J/K)
S, power spectral density (PSD) (m^2)
T, absolute temperature (K)
t, time (s)
u, gas velocity along x-axis (m/s)
x, spatial distance along x-axis (m)
W, one-sided power spectral density (m^2)
w, shock speed (m/s)
w_j, gas dynamics variables.

Greek Symbols

α, parameter for shock initialization
ε, distance from the wall for shock reflection
γ, ratio of specific heats
$\delta \equiv (\gamma - 1)/2$
Δ [illegible]
Δx, finite difference increments of x
ξ, damping coefficient
Λ, eigenvalue matrix of J
λ_j, characteristic speeds
$\pi = 3.14159...$
ρ, density (Kg/m^3)
$\Sigma \equiv (R_{jB} - R_{jA})/a_A$
$\Sigma^* \equiv (a_B \pm \delta(u_B - u_A))/a_A$
σ^2 variance of sampled time series (m^2)
ω, circular frequency (rad/s).

Superscripts

k, time level.

Subscripts

A, shock low pressure side
B, shock high pressure side
o, initial conditions
j, grid point
j', $=j+1$
M_s, derivative with respect to shock Mach number
n, grid point
$p.w.$, present work
r, reference
s, shock
t, time derivative
x, space derivative.

Operator's Symbols

$d(\cdot)/dx$, first-order space derivative
$d^2(\cdot)/dx^2$, second-order space derivative
$d(\cdot)/dt$, first-order time derivative
$D(\cdot)/Dt$, substantial derivative.

ACKNOWLEDGMENTS

This problem was suggested to the authors by Professor Gino Moretti. The authors would also like to thank Professor Moretti for illuminating discussions and comments. This work was partially performed at the G.M.A.F. Inc., Freeport, New York.

REFERENCES

1. J. D. BAUM AND J. N. LEVINE, *J. Comput. Phys.* **58**, 1 (1985).
2. J. D. BAUM AND J. N. LEVINE, *AIAA J.* **20**, 955 (1982).
3. J. N. LEVINE AND J. D. BAUM, *AIAA J.* **21**, 557 (1983).
4. G. MORETTI, *Comput. Fluids* **7**, 191 (1979).
5. G. MORETTI, *Comput. Fluids* **15**, 59 (1987).
6. R. D. RICHTMYER AND K. W. MORTON, *Difference Methods for Initial-Values Problems* (Interscience, New York, 1967).
7. G. MORETTI AND M. ABBETT, *AIAA J.* **5**, 1557 (1967).
8. M. D. SALAS, *AIAA J.* **14** (1976).
9. G. MORETTI AND M. T. DI PIANO, NASA Contractor Report No. 3712, 1983 (unpublished).
10. I. L. CHERN, J. GLIMM, O. MCBRYAN, B. PLOHR, AND S. YANIV, *J. Comput. Phys.* **62**, 83 (1986).
11. M. DI GIACINTO AND M. VALORANI, *Comput. Fluids* **17**, 1 (1989); presented at *Symposium on Physical Aspects of Numerical Gas Dynamics, Polytechnic University, Farmingdale, New York*, 1987.
12. G. MORETTI AND M. VALORANI, in *Proceedings, VIIth GAMM Conference Numerical Method in Fluid Mechanics, Louvain-la-Neuve, Belgium, 1987*, edited by Deville (Vieweg, Brunswick, 1987), p. 239.

13. P. M. MORSE AND K. V. INGARD, *Theoretical Acoustics* (McGraw–Hill, New York, 1968), p. 874.
14. G. MORETTI AND X-C. ZHONG, *Comput. Fluids* **10**, 277 (1982).
15. G. RUDINGER, *Non Steady Duct Flow: Wave Diagram Analysis* (Dover, New York, 1969).
16. R. COURANT AND K. O. FRIEDRICHS, *Supersonic Flow and Shock Waves* (Interscience, New York, 1948).
17. A. H. SHAPIRO, *Compressible Fluid Flows* (Ronald Press, New York, 1954).
18. D. E. NEWLAND, *An Introduction to Random Vibrations and Spectral Analysis* (Longman, London/New York, 1975).
19. G. MORETTI, "The Choice of a Time-Dependent Technique in Gas Dynamics," Polytechnic Institute of Brooklyn Report, PIBAL 69-26, 1969 (unpublished).
20. G. MORETTI, "A Short Course in Numerical Gas Dynamics," Polytechnic Institute of New York, March 11–15, 1985, pp. 52–80 (unpublished).